Int. J. Heat Mass Transfer. Vol. 36, No. 6, pp. 1541–1551, 1993
Printed in Great Britain

0017-9310/93 $6.00+0.00

Numerical simulation of subcooled boiling and heat transfer in vertical ducts

J. C. LAI
Public Service Electric and Gas Company, Hancock's Bridge, NJ 08038, U.S.A.

and

B. FAROUK
Department of Mechanical Engineering and Mechanics, Drexel University, Philadelphia, PA 19104, U.S.A.

(*Received* 15 *November* 1991 *and in final form* 7 *July* 1992)

Abstract—A two-dimensional two-phase non-equilibrium model is presented to predict the void fraction distribution, flow and temperature fields for turbulent subcooled flow boiling at elevated pressures in heated vertical ducts (pipes and channels). The model is based on the conservation of mass, momentum, and energy equations for each of the two phases. Appropriate wall and interfacial conditions are formulated to close the problem. The non-equilibrium temperature and velocity distributions of the two phases and void fraction profiles show considerable variation along the radial and axial directions for the subcooled flow boiling cases considered. The effects of inlet subcooling, exit pressure and wall heat flux on the flow boiling behavior were predicted. The predicted radially averaged void fractions are compared with the experimental results available in the literature. The radial temperature distributions and void fraction profiles are also compared with available experimental measurements.

1. INTRODUCTION

THE PREDICTION of the void fractions in subcooled boiling flow in vertical pipes and channels has been the subject of numerous studies. In the slightly subcooled region, attempts were made to analytically predict the point of departure of the vapor bubbles or net vapor generation [1–4]. Levy [1] employed a criterion for bubble detachment based on the force balance on a bubble. Saha and Zuber [3] were able to predict the net vapor generation based on the experimental boiling data. In the highly subcooled region, empirical relations and heat balance in the fluid were employed to predict the void fractions [5–7]. The empirical relations are based on the wall superheating, pressure, and heat flux [7].

Results of most of these methods are in good agreement with the experimental data on the radially averaged void fractions for the parameter ranges in which these studies are based. The above models, however, do not provide any information on the distribution of the void fraction, velocity and non-equilibrium temperatures of the two phases along the transverse direction. It was observed in the past studies with heated vertical pipes or channels that appreciable subcooling existed in the liquid core downstream from the point of vapor generation; and vapor phase was mostly found adjacent to the heated wall. Both from visual observations and measurements, it is also confirmed that a non-uniform temperature field exists across the diameter of the pipe or the width of the channel [8, 9]. Larsen and Tong [10] employed the 'bubble layer' method to predict the void fraction and temperature distribution in a heated pipe. However, only the radially averaged void fractions along the axial direction were reported. The application of detailed two-fluid models to the solution of subcooled boiling problems has just began. Recently, Kurul and Podowski [11] employed a two-fluid model to predict the void fraction distribution in subcooled flow boiling. The energy equation for the liquid phase was only considered. A new correlation for the coolant enthalpy at void detachment point in developing flows was proposed, and various effects of unsteady flow and heat transfer conditions on void distribution in a channel were investigated.

In this paper, following Kurul and Podowski [11], numerical results are presented for the turbulent water-steam non-equilibrium flow in a vertical pipe and a rectangular channel. The liquid phase and the vapor phase characteristics due to subcooled boiling are predicted by solving the modeled two-dimensional governing equations using a finite difference scheme. Interfacial relations including the mass, momentum and heat transfer used to couple the liquid and vapor phases are considered. In the present model the liquid phase turbulence is characterized via a k–ε model where the governing equations for k and ε were solved simultaneously with the other transport variables considered in the problem. The two-phase effects on the turbulence characteristics can be realized in the above method. Kurul and Podowski [11] characterized the

NOMENCLATURE

A	area per unit volume
A_{flow}	flow area
C_d	drag coefficient
d	bubble diameter
$\bar{F}_{i\text{-}int}$	interfacial force per unit volume
$\bar{F}''$	interfacial force per unit area
f	friction factor
g	acceleration due to gravity
h	enthalpy
h_{fg}	latent heat of vaporization
$J_{i\text{-}int}$	interfacial heat source/sink term for the enthalpy equation
k	kinetic energy of turbulence (liquid phase)
$\dot{M}$	interfacial mass transfer rate per unit volume
p	pressure
Pr	Prandtl number
$q_{i\text{-}int}$	interfacial heat transfer per unit volume
R	volume fraction
Re_b	bubble Reynolds number, $d \cdot V_{rel}/v$
Re_c	cell Reynolds number, $(\Delta r)w/v$
T	temperature
$\bar{V}$	velocity vector
v	radial velocity component
w	axial velocity component.

Greek symbols

Γ	momentum exchange coefficient, $v_l + v_t$
Γ_h	energy exchange coefficient, $v_l/Pr_l + v_t/Pr_t$
ε	dissipation rate of turbulent kinetic energy
λ	interfacial heat transfer coefficient
v_t	turbulent viscosity
v_l	kinematic viscosity
ρ	density.

Subscripts

i	phase index
g	vapor phase
f	liquid phase
sat	saturation
int	interfacial
vis	viscous friction
rel	relative.

liquid phase turbulence by a 'frozen' k–ε model where the transport equations for k and ε were solved *a priori* from a single-phase flow problem.

2. PROBLEM DESCRIPTION

Subcooled convective flow boiling was considered in an axisymmetric vertical heated pipe and in a two-dimensional vertical heated channel. A schematic of the heated vertical pipe is shown in Fig. 1. Subcooled water enters the pipe from the bottom. Uniform heat flux boundary conditions are applied along the pipe wall. A 0.024 m diameter pipe is considered and the inlet mass flux (of the subcooled liquid) is held at 890 kg m^{-2} s^{-1}. A 2.0 m length section of the pipe is considered for the computations. Specified pressure condition was applied to the exit of the pipe. The numerical simulations were done at three pressure levels, namely, 1.5, 3.0, and 4.5 MPa. For each pressure level, two values of the wall heat flux were considered, namely 380 and 790 kW m^{-2}. These test cases are chosen so that the predictions can be compared with the experimental results from Bartolemei and Chanturiya [8]. The inlet (equilibrium) qualities and calculated subcooling and temperatures are shown in Tables 1–3.

For the vertical duct, a 0.011 m wide section is considered and the inlet mass flux (of the subcooled liquid) is held at 950 kg m^{-2} s^{-1}. A 1.0 m length section of the duct is considered for the computations. A specified pressure condition was applied to the exit of the duct as before. The numerical simulations were done at two pressure levels, namely, 2.72 and 4.0 MPa. These test cases are again chosen so that the

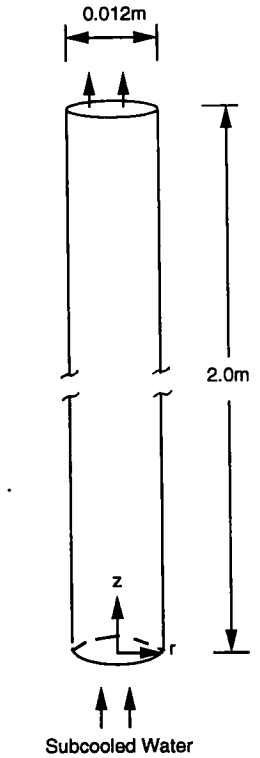

FIG. 1. Schematic of the problem geometry.

Table 1. Description of test cases 1a and 1b (pressure 1.5 MPa; inlet mass flux 890 kg $m^{-2} s^{-1}$)

	Case 1a	Case 1b
Inlet quality	−0.0523	−0.1178
Inlet subcooling	22.6°C	50.9°C
Inlet temperature	177.4°C	149.1°C
Heat flux, kW m^{-2}	380	790

Table 2. Description of test cases 2a and 2b (pressure 3.0 MPa; inlet mass flux 890 kg $m^{-2} s^{-1}$)

	Case 2a	Case 2b
Inlet quality	−0.0655	−0.1365
Inlet subcooling	25.0°C	48.1°C
Inlet temperature	210.0°C	186.9°C
Heat flux, kW m^{-2}	380	790

Table 3. Description of test cases 3a and 3b (pressure 4.5 MPa; inlet mass flux 890 kg $m^{-2} s^{-1}$)

	Case 3a	Case 3b
Inlet quality	−0.0702	−0.1523
Inlet subcooling	24.0°C	50.0°C
Inlet temperature	231.0°C	205.0°C
Heat flux, kW m^{-2}	380	790

Table 4. Description of test case 4

Pressure	2.72 MPa
Inlet mass flux	950 kg $m^{-2} s^{-1}$
Inlet subcooling	4.5°C
Heat flux, kW m^{-2}	216

Table 5. Description of test case 5

Pressure	4.0 MPa
Inlet mass flux	950 kg $m^{-2} s^{-1}$
Inlet subcooling	2.3°C
Heat flux, kW m^{-2}	280

predictions can be compared with the experimental results from St Pierre and Bankoff [9]. A rectangular channel with 0.011×0.044 m cross-section was considered in the above study. The inlet (equilibrium) qualities and calculated subcooling and temperatures are shown in Tables 4 and 5.

3. MATHEMATICAL MODEL

The mass, momentum and energy conservation equations were applied for each of the phases. The conservation equations for the two-fluid non-equilibrium (TFNE) model in the r–z coordinates are summarized as follows. (Similar equations in Cartesian coordinates, x–z, were employed for the vertical duct predictions. These are not repeated in this paper.)

The mass conservation equation for each phase:

$$\frac{1}{r}\frac{\partial}{\partial r}(rR_i\rho_i v_i)+\frac{\partial}{\partial z}(\rho_i R_i w_i)=\dot{M}_i. \quad (1)$$

The r-direction momentum equation:

$$\frac{1}{r}\frac{\partial}{\partial r}(rR_i\rho_i v_i^2)+\frac{\partial}{\partial z}(R_i\rho_i w_i v_i)= -R_i\frac{\partial p}{\partial r}+\frac{2}{r}\frac{\partial}{\partial r}\left(r\rho_i R_i\Gamma_i\frac{\partial v_i}{\partial r}\right)+\frac{\partial}{\partial r}\left(\rho_i R_i\Gamma_i\frac{\partial v_i}{\partial z}\right) +\frac{\partial}{\partial z}\left(\rho_i R_i\Gamma_i\frac{\partial w_i}{\partial z}\right)-\frac{2\rho_i R_i v_i\Gamma_i}{r^2}+F^r_{i\text{-}int}. \quad (2)$$

The z-direction momentum equation:

$$\frac{1}{r}\frac{\partial}{\partial r}(R_i\rho_i r v_i w_i)+\frac{\partial}{\partial z}(R_i\rho_i w_i^2)= -R_i\frac{\partial p}{\partial z}+\frac{1}{r}\frac{\partial}{\partial r}\left(\rho_i R_i r\Gamma_i\frac{\partial w_i}{\partial r}\right)+2\frac{\partial}{\partial z}\left(R_i\rho_i\Gamma_i\frac{\partial w_i}{\partial z}\right) +\frac{1}{r}\frac{\partial}{\partial r}\left(R_i\rho_i\Gamma_i r\frac{\partial v_i}{\partial r}\right)+R_i\rho_i g+F^z_{i\text{-}int}. \quad (3)$$

The liquid phase momentum diffusion coefficient Γ_f includes the laminar and turbulent contributions (v_l+v_t). An estimate for the liquid phase v_t is obtained locally by employing the k–ε model.

The energy equation:

$$\frac{1}{r}\frac{\partial}{\partial r}(\rho_i R_i r v_i h_i)+\frac{\partial}{\partial z}(\rho_i R_i w_i h_i)= \frac{1}{r}\frac{\partial}{\partial r}\left(r\rho_i R_i\Gamma_{h_i}\frac{\partial h_i}{\partial r}\right)+\frac{\partial}{\partial z}\left(R_i\rho_i\Gamma_{h_i}\frac{\partial h_i}{\partial z}\right)+J_{i\text{-}int}. \quad (4)$$

The liquid phase energy exchange coefficient is obtained as $\Gamma_{hf}=v_l/Pr_l+v_t/Pr_t$ where Pr_l and Pr_t are the laminar and turbulent Prandtl numbers, respectively. A Pr_t value of unity was used for the present calculations.

The detailed descriptions of the interfacial relations, $\dot{M}_i$, $\bar{F}_{i\text{-}int}$ and $J_{i\text{-}int}$ are presented in Section 4.

The turbulence model for the liquid phase

A k–ε turbulent model is applied to the liquid phase to calculate the turbulent viscosity. No turbulence model was applied to the vapor phase since the gas has significantly lower density and momentum compared to the liquid phase for the problems considered. The generalized governing equation for k and ε is described as follows:

$$\frac{\partial}{\partial t}(R_f\rho_f\phi)+\frac{1}{r}\frac{\partial}{\partial r}(R_f\rho_f r v_f\phi)-\frac{\partial}{\partial z}\left(\rho_f R_f\frac{\Gamma_f}{\sigma_\phi}\frac{\partial\phi}{\partial z}\right)$$
$$-\frac{1}{r}\frac{\partial}{\partial r}\left(r\rho_f R_f\frac{\Gamma_f}{\sigma_\phi}\frac{\partial\phi}{\partial z}\right)=S_\phi \quad (5)$$

where 'ϕ' represents either k or ε, S_ϕ is the source term for either k or ε, index f represents the liquid phase. The source terms for k and ε are given as $S_k = R_f(G_k-\rho_f\varepsilon)$

$$S_\varepsilon = R_f\varepsilon/k(C_1G_k-C_2\rho_f\varepsilon)$$

where

$$G_k=\rho v_t\left[2\left(\frac{\partial w_f}{\partial z}\right)^2+\left(\frac{\partial v_f}{\partial r}\right)^2+\left(\frac{v_f}{r}\right)^2+\left(\frac{\partial w_f}{\partial r}+\frac{\partial v_f}{\partial z}\right)^2\right].$$

The model constants were assigned the same values as in the single-phase flows ($C_1 = 1.44$, $C_2 = 1.92$, $C_\mu = 0.09$, $\sigma_k = 1.0$, $\sigma_\varepsilon = 1.3$).

Boundary conditions

Calculations were carried out for one-half of the flow region in the r–z plane assuming symmetry conditions (Fig. 1). For the vertical duct, the calculations were carried out for one-half of the channel width and along the channel length (in the x–z plane). At the inlet, the mass flux and axial velocity of both phase are specified. The inlet enthalpies are calculated using the equilibrium quality information from Tables 1–5. The inlet k and ε values are calculated assuming small levels of turbulence of the incoming flow. At the outlet, the pressure is specified as shown in Tables 1–5. Zero gradients for k and ε are specified at the outlet.

In the present TFNE model, the velocity and thermal boundary layers near the wall are not explicitly resolved. The wall shear stress and heat flux are modeled using phenomenological approach and are substituted in the momentum and energy equations are sink/source terms for the near wall nodes.

The turbulent wall friction force is supplied to the momentum equation for the liquid phase. The friction force is given as

$$F_w = -f\cdot\rho_f\cdot A_{flow}\cdot w_f^2\cdot R_f \quad (6)$$

where ρ_f is the density of the liquid, A_{flow} is the flow area (the cross-sectional area of the cell near the wall), and w_f is the axial velocity component. The friction factor is based on the logarithmic law [12],

$$f=[0.435/\ln(1.01+9(Re_c)\cdot f^{0.5})]^2. \quad (7)$$

In the above relation, cell Reynolds number Re_c is based on the half distance from the wall to the first cell (Δr or Δx). The friction factor f is solved iteratively in the overall calculations.

The shear stress for the vapor phase near the wall is neglected. This can be justified for subcooled boiling where the bubbles slide in the laminar sublayer in the flow direction. Standard wall function boundary conditions are used to calculate the liquid phase k and ε at the near wall points.

At the pipe surface or wall, constant heat flux condition is considered and the values used are specified in Tables 1–5. Heat flux is added to the liquid energy equation. For the subcooled flow boiling, the walls are mostly in contact with the liquid phase. Any boiling in the near wall cell is accommodated by the interfacial heat transfer (described in the next section). The effects of a more complex distribution of wall heat flux (considering boiling and quenching heat flux due to detached bubbles) as suggested by Kurul and Podowski [11] are also considered.

Along the center line of the problem geometries, the gradients of the velocity and enthalpy of each phase is zero to satisfy the symmetry condition. The gradients of liquid phase k and ε are also set to zero along the center line.

4. AUXILIARY FORMULATIONS

Interfacial momentum transfer

The interfacial momentum transfer can be expressed as the product of the interfacial friction force per unit area multiplied by the interfacial area concentration (interfacial area per unit volume). The interfacial friction force (from liquid to interface) per unit area is described as

$$\bar{F}''_{f\text{-}int} = C_d\rho_f\bar{V}_{rel}\cdot\bar{V}_{rel}R_g \quad (8)$$

where C_d is the interfacial drag coefficient and is taken [13] as the minimum of

$$1.0 \quad \text{and} \quad 24(1.0+0.1(Re_b)0.75)/Re_b.$$

Here $\bar{V}_{rel}$ is the velocity difference between the two phases and Re_b is the Reynolds number based on the bubble diameter and the relative velocity. The bubble diameter was taken as a constant value of 1 mm. Consideration of the bubble diameter as a local function of subcooling produced little difference in the void fraction predictions.

The interfacial area per unit volume is assumed to be linearly proportional to the void fraction. The expression used is

$$A_{int} = R_gC$$

where C is 700 $m^2\ m^{-3}$ for the subcooled region [14] and R_g is the void fraction.

The interfacial momentum transfer (from liquid to interface) per unit volume is given as

$$\bar{F}_{f\text{-}int} = \bar{F}''_{f\text{-}int}A_{int}. \quad (9)$$

To satisfy the overall momentum balance between the two phases,

$$\bar{F}_{g\text{-}int} = -\bar{F}_{f\text{-}int}.$$

Interfacial heat and mass transfer

Consideration of the interfacial heat transfer is more involved than the interfacial momentum transfer

due to the presence of boiling and/or condensation. For the present calculations the wall heat flux is transferred to the liquid phase for the near wall node; therefore the phase change is primarily controlled by the liquid–interface heat transfer. The heat transfer process within each computational cell is due to the interaction with the neighboring cells for the same phase and interaction between the phases within the same cell. In mathematical form, the interfacial heat transfer per unit volume from liquid to the interface is expressed as

$$q_{f\text{-}int} = \lambda_{f\text{-}int} A_{int} (T_f - T_{sat}) \tag{10}$$

where $q_{f\text{-}int}$ is the interfacial heat transfer from liquid to interface, A_{int} is the interfacial area per unit volume as described previously and $\lambda_{f\text{-}int}$ is the interfacial heat transfer coefficient. The heat transfer coefficient between the interface and the liquid phase is given in refs. [15, 16].

Heat transfer from vapor to the interface is small since the vapor temperature remains almost unchanged in this study. The interfacial heat transfer from vapor to interface is expressed as

$$q_{g\text{-}int} = \lambda_{g\text{-}int} A_{int} (T_g - T_{sat}) \tag{11}$$

where $\lambda_{g\text{-}int}$ is the heat transfer coefficient between the interface and the gas phase. A sensitivity study was made using different values of vapor interfacial heat transfer coefficients. The range of the values were from a few hundreds (W $m^{-2} C^{-1}$) to a few thousands (W $m^{-2} C^{-1}$). The effect on the results is negligible. The dominant interfacial heat transfer stems from the liquid side and not from the vapor side for the cases considered.

The interfacial mass transfer rate is obtained by the heat balance at the vapor–liquid interface. The interfacial mass transfer rate per unit volume becomes

$$\dot{M}_f = (q_{g\text{-}int} - q_{f\text{-}int})/h_{fg} \tag{12}$$

where h_{fg} is the latent heat of vaporization at the given pressure. In the vapor mass conservation equation, the source term is $\dot{M}_g$. To satisfy the 'overall' mass balance equation,

$$\dot{M}_f = \dot{M}_g.$$

The interfacial heat source/sink added to the liquid enthalpy equation (4) is then expressed as

$$J_{f\text{-}int} = q_{f\text{-}int} + \dot{M}_f (h_f - h_{f,sat}) \tag{13}$$

where $q_{f\text{-}int}$ is the interfacial heat transfer from the liquid to the interface in a computational cell and $\dot{M}_f(h_f - h_{f,sat})$ is the energy loss due to the mass change (or phase change) of the liquid. Similarly, the net interfacial heat source/sink term for the vapor phase is expressed as

$$J_{g\text{-}int} = q_{g\text{-}int} + \dot{M}_g (h_g - h_{g,sat}). \tag{14}$$

Consideration of the wall heat flux

The wall heat flux was partitioned into three components by Kurul and Podowski [11] for the prediction of subcooled flow boiling. The three components are the single phase convection, quenching due to the cold liquid that fills the space vacated by the vapor phase, and boiling of liquid. These components were calculated using the empirical relations given in ref. [11] prior to solving the two-fluid conservation equations. In the present study, the wall heat flux partition is considered by employing the interfacial heat transfer relations in the near wall cell. Instead of directly using an empirical relation for wall boiling [11], the boiling in the near wall computational cell is obtained via the interfacial heat transfer relations. The liquid phase convection and the so-called quenching heat-flux are not separately calculated in the present method. The net effect to the liquid phase energy equation is however, obtained by subtracting the wall heat flux from the interfacial heat transfer that causes boiling. The quenching heat-flux was not explicitly considered due to the lack of an adequate model. The quenching heat flux model given by Del Valle and Kenning [17] contains a large number of experimentally measured parameters. The present method also eliminates the need to explicitly evaluate single phase convective heat flux to the liquid outside the zone of influence of the bubbles.

5. NUMERICAL MODEL

A numerical iterative scheme is used to obtain the solutions after all boundary conditions for the two phases are prescribed. A staggered grid system was used where the velocities were stored on cell faces and R_i, h_i, p, k and ε are stored at cell centers. The PHOENICS code [18] was used as the numerical solver for the difference equations. The variables R_i, $\bar{V}_i$, h_i, p, k and ε are solved using the IPSA (interphase-slip-algorithm) [19]. The computations were carried out on an IBM 3090 machine located at Drexel University.

6. RESULTS AND DISCUSSIONS

The model described above was applied to predict the void fraction, velocity and temperature fields for subcooled flow boiling in a vertical pipe and a vertical channel for different flow and wall heat flux conditions. Specifically six cases were considered for the vertical pipe as shown in Tables 1–3. An exit pressure of 1.5 MPa is considered for cases 1a and b; 3.0 MPa for cases 2a and b; and 4.5 MPa for cases 3a and b. Lower inlet subcooling and lower wall heat flux were considered for cases 1a, 2a, and 3a. Higher inlet subcooling and higher wall heat flux were given to cases 1b, 2b, and 3b. The effects of the exit pressure, inlet subcooling and wall heat flux on the subcooled

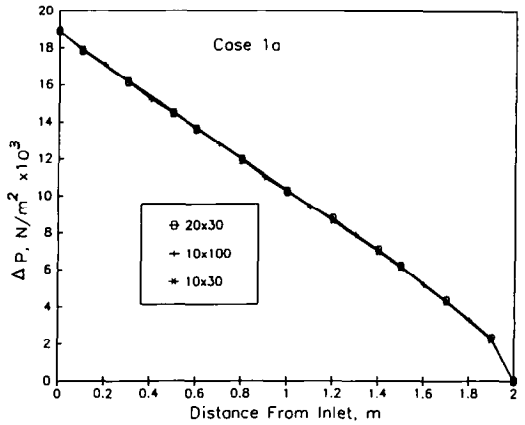

FIG. 2. Comparison of pressure drop prediction using different mesh sizes for case 1a.

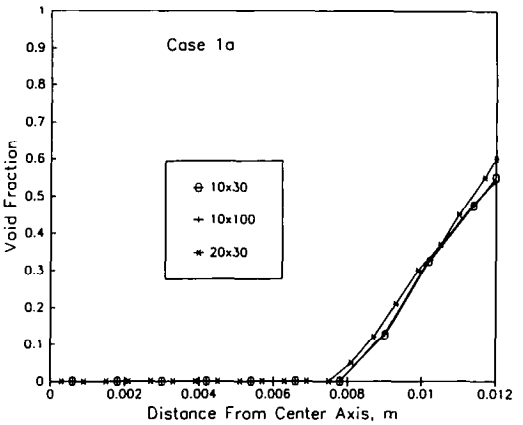

FIG. 4. Comparison of void fraction distribution using different mesh sizes for case 1a (at $z = 1.8$ m).

flow boiling can be determined from the results of these cases. Two cases were considered for the heated vertical channel. An exit pressure of 2.72 MPa is considered for case 4 and 4.0 MPa for case 5.

Sensitivity study using different mesh sizes

Computations were first performed for a specific case (case 1a as shown in Table 1) using different mesh sizes. The three different mesh sizes were 10×30, 10×100 and 20×30 ($r \times z$) for the computational domain having a radius of 0.012 m and a length of 2.0 m. The results for the axial pressure drop, the liquid velocity distribution, at $z = 1.8$ m and the void fraction distribution at the same height are shown in Figs. 2–4, respectively. The results indicate that a finer mesh in the axial direction produced little variations in the predictions. A 10×30 mesh size was found to be a good compromise between the desired accuracy and computational time.

Radial void, temperature and superficial velocity distributions

The predicted radial void fraction profiles at two axial locations ($z = 1.1$ and 2.0 m) are shown in Figs. 5 and 6 for cases 1a and 1b (1.5 MPa exit pressure), respectively. The void fraction becomes higher at higher elevations as expected. The void fractions increases rapidly near the wall while the center part of the pipe is still in the subcooled state for the two cases. For the same pressure conditions, the void frac-

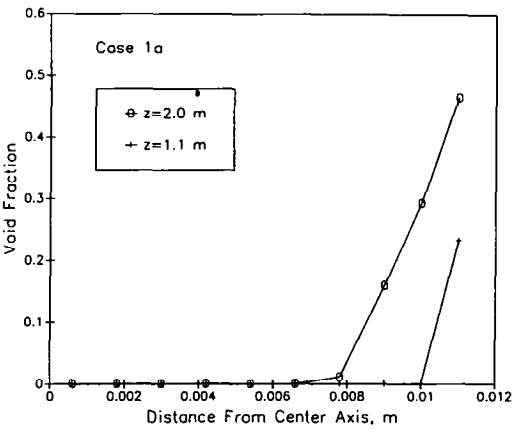

FIG. 5. Void fraction profiles at two elevations for case 1a.

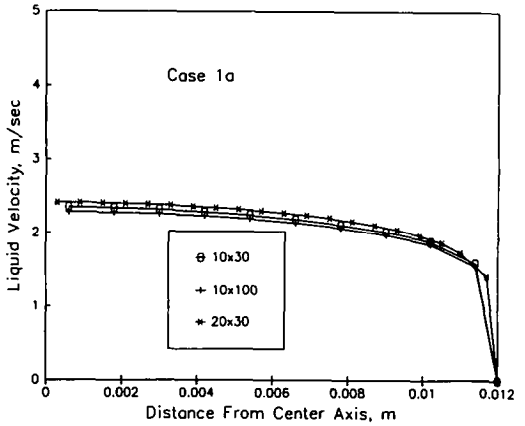

FIG. 3. Comparison of liquid velocity distribution using different mesh sizes for case 1a (at $z = 1.8$ m).

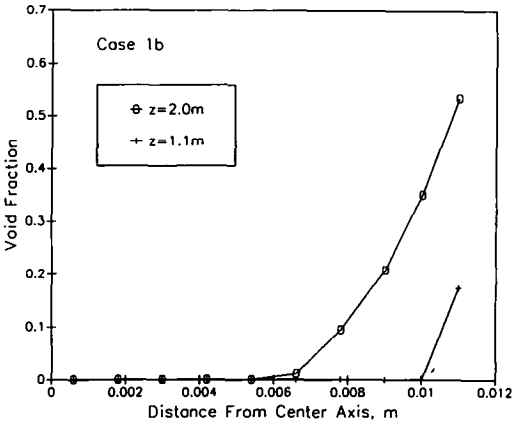

FIG. 6. Void fraction profiles at two elevations for case 1b.

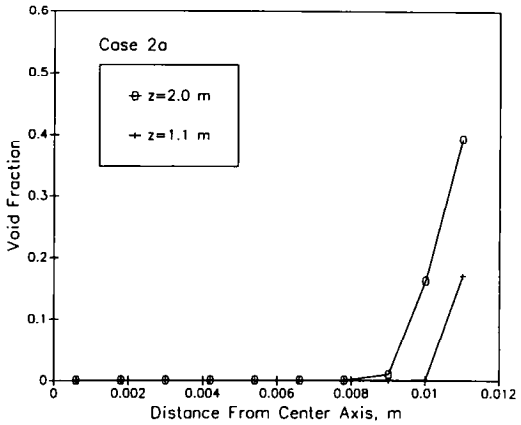

FIG. 7. Void fraction profiles at two elevations for case 2a.

tion becomes higher for the higher heat flux. The radial void fraction distribution for the case 2a (3.0 MPa exit pressure) is shown in Fig. 7. For the same inlet subcooling and heat flux boundary conditions, the predicted void fractions are higher for the lower pressure cases (Fig. 5 vs Fig. 7).

The predicted transverse void fraction distributions for case 4 (the vertical channel) at three axial locations are shown in Fig. 8. The measured void fractions at equivalent vertical locations are also shown in this figure [9]. The experimental data show considerable scatter, particularly at high void fraction regions. It is, however, seen that the overall agreement between the predictions and the measurements is good. In both cases the void fractions are higher near the walls and gradually fall off towards the axis.

The radial liquid temperature profiles for case 1a are shown in Fig. 9 at two axial locations. The non-equilibrium effects are evident. The middle part of the pipe is in subcooled state (even at $z = 2.0$ m) while the region near the wall is slightly superheated. The level of subcooling is found to diminish along the length of the pipe. The radial liquid temperature profiles for case 2b at various axial locations are shown in Fig. 10. The measured temperature distributions [8] at equivalent vertical locations are also shown in the same figure. The agreement between the predictions and measurements are excellent.

The superficial axial velocities ($R_g \cdot w_g$) of the vapor phase near the exit of the pipe at $z = 1.8$ m for cases 1a, 2a, and 3a are shown in Fig. 11. With increasing pressure the boiling rate decreases; hence the decrease of superficial vapor velocity between cases 1a, 2a, and 3a. The vapor phase is found to be high near the wall and the highest superficial velocity is found at the location closest to the wall. The corresponding superficial liquid velocity distributions are shown in Fig. 12. The velocity distribution (not shown) is similar to that observed in single phase flows since the liquid is at subcooled conditions near the center of the pipe. The liquid velocities are small near the wall due to the wall friction and void formation. For the same mass

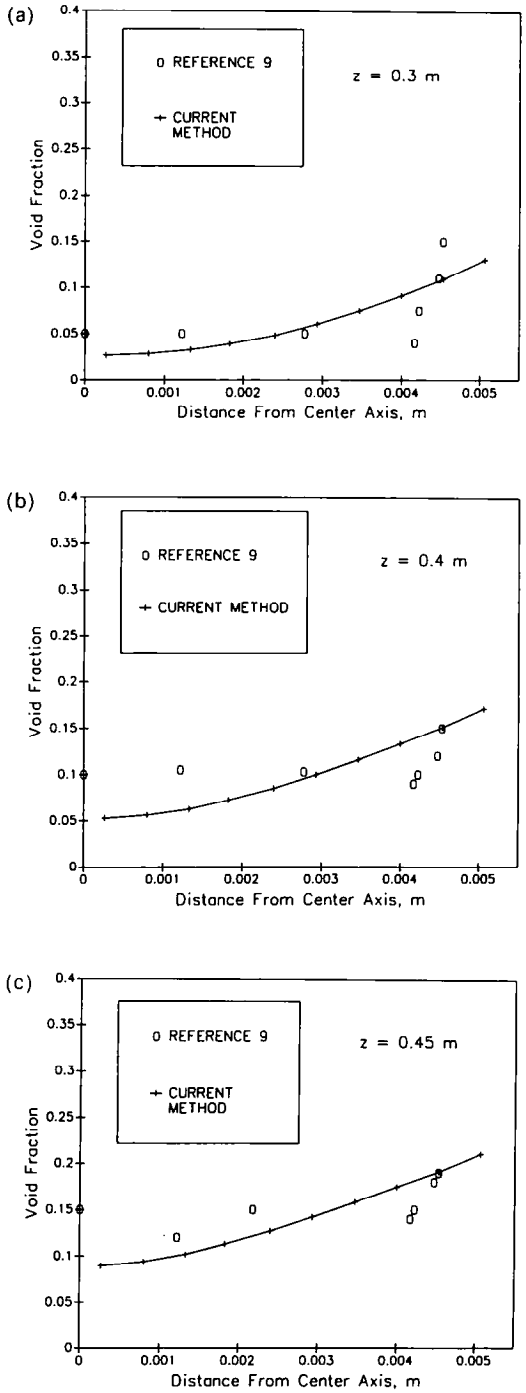

FIG. 8. Comparison of transverse void fraction distributions for case 4. (a) $z = 0.3$ m; (b) $z = 0.4$ m; (c) $z = 0.45$ m.

flow rate, the liquid velocity also decreases substantially for the higher exit pressure cases.

Radially/transversally averaged void fraction along axial direction

The radially averaged void fractions across the pipe versus axial distance are shown in Figs. 13 and 14 for all the six test cases described in Tables 1–3. Figures 13(a)–(c) show the comparisons of the predicted radi-

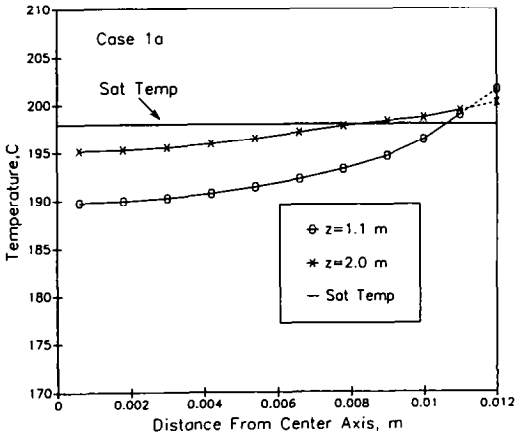

FIG. 9. Liquid temperature profiles at two elevations for case 1a.

ally averaged void fractions with measurements [8] and predictions given by Larsen and Tong [10] for the cases with the low wall heat flux (380 kW m^{-2}). Similar comparisons are shown in Figs. 14(a)–(c) for cases with the higher wall heat flux (790 kW m^{-2}).

The experiments of Bartolemei and Chanturiya [8] were performed by first establishing the no void condition by running water only through the test section. Subsequently, void conditions were established at conditions described in Tables 1–3. A gamma detector was used as a measuring device in these experiments. Different counting rates were obtained at different void conditions. Comparing the counting rates at the heating conditions to those at no heating condition (water only), the radially averaged void fraction can be determined. It is interesting to note that past analytical and experimental work on subcooled boiling (including refs. [8] and [9]), report radial void and temperature distributions as well as radially averaged void fraction as a function of equilibrium qualities or average subcooling instead of the axial length. The axial length, however, can be recovered from the equilibrium quality or the average subcooling by using a one-dimensional heat balance to the problem geometry. This trend in the past was perhaps due to the exclusive use of one dimensional equilibrium models in characterizing boiling in channels or pipes. In the present calculations, the predictions are given directly as a function of axial length. The experimental void fraction data [8] and the one-dimensional model predictions from Larsen and Tong [10] are also shown as a function of the axial distance in Figs. 13 and 14.

The predicted locations of the initial void formation are shown in Figs. 13 and 14. The radially averaged void fractions from the present analysis are somewhat lower than the experimental data [8] at the bottom half of the pipe. The predictions at the upper half of the pipe are, however, in good agreement with the data. Since the experimental data were originally reported as a function of equilibrium quality, it is not surprising to note that higher void fractions are

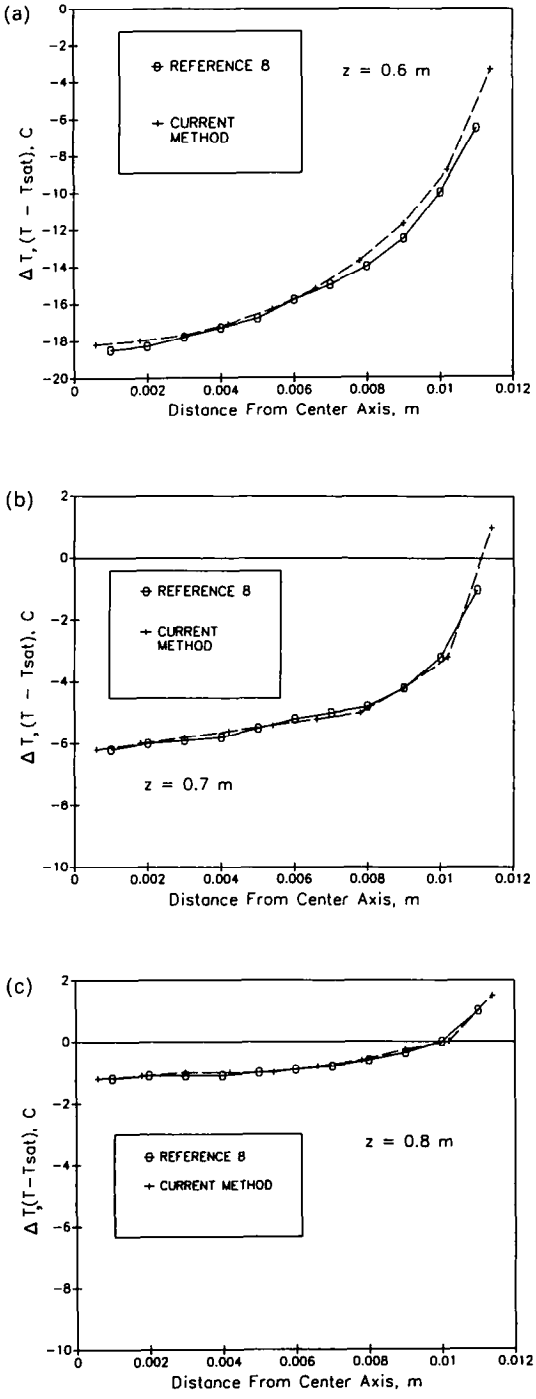

FIG. 10. Comparison of radial liquid temperature distributions at different axial locations for case 2b. (a) $z = 0.6$ m; (b) $z = 0.7$ m; (c) $z = 0.8$ m.

reported in ref. [8] near the location of the void incipience. Our predictions show that considerable void variation exists radially near the entrance of the pipe and the non-equilibrium effects are also significant in this region. Similar trends are also observed for the one-dimensional model predictions. The effect of subcooling (non-equilibrium state) is pronounced near the location of the incipience of void formation. According to the present model, the predicted location

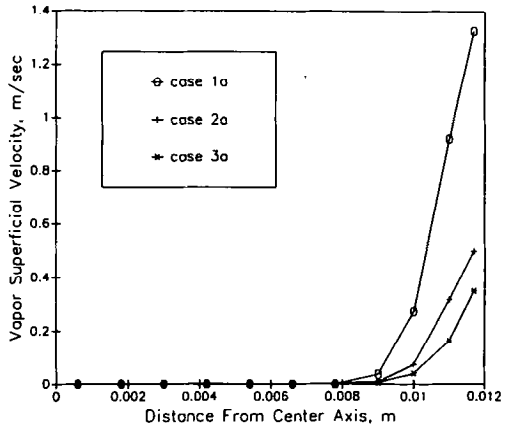

FIG. 11. Predicted vapor superficial velocity distribution across the pipe at $z = 1.8$ m (for cases 1a, 2a, and 3a).

of the incipience of the void formation at different pressures is about the same for the same inlet subcooling and wall heat flux conditions.

For the vertical channels, the transversally averaged void fraction as a function of the axial distance for cases 4 and 5 are shown in Figs. 15 and 16, respectively. The rate of void fraction increase is slower for case 4 compared to case 5 due to higher inlet subcooling and lower wall heat flux in case 4. The predicted void fractions are in good agreement with the experimental data.

Finally the predicted radially averaged void fractions are compared with the model predictions of Kurul and Podowski [11] in Fig. 17 for a specific case. The diameter of the vertical test channel was 0.0154 m, the wall heat flux was 570 kW m^{-2}, and the inlet mass flux was 900 kg $m^{-2} s^{-1}$ at 4.5 MPa. The experimental data of Bartolemei and Chanturiya [8] are also shown in the figure. In the present method the interfacial source/sink terms were added to both the gas phase and liquid phase equations. The effects of bubble detachment and quenching on the radially averaged void profiles are found to be insignificant.

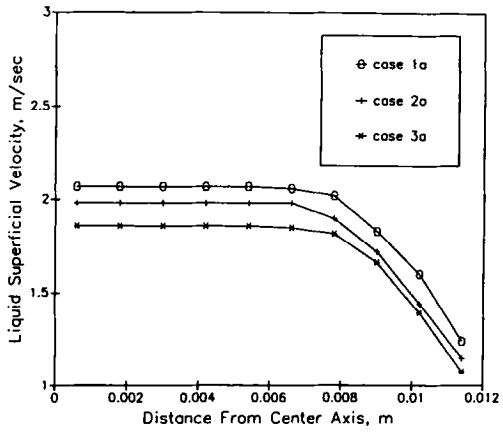

FIG. 12. Liquid superficial velocity distribution across the pipe at $z = 1.8$ m (for cases 1a, 2a, and 3a).

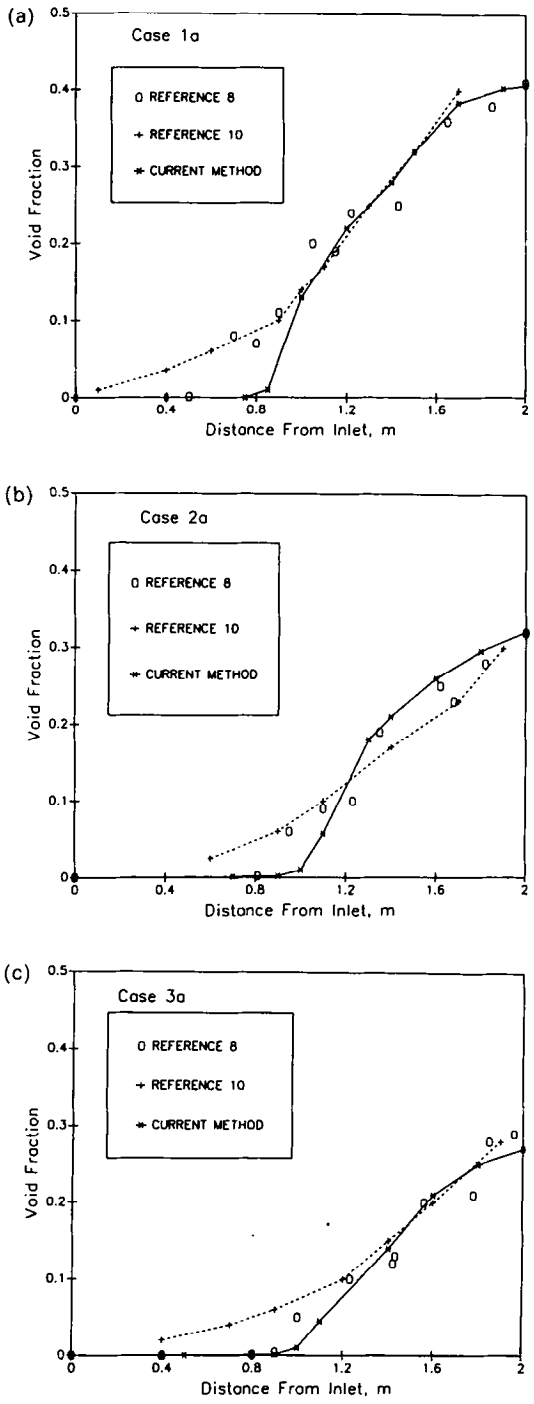

FIG. 13. Comparison of the radially averaged void fraction predictions. (a) Case 1a; (b) case 2a; (c) case 3a.

7. CONCLUSIONS

With the advancement of the multi-dimensional two-fluid models with proper closure information, the non-equilibrium and multi-dimensional effects of the void distribution and temperature profile across the pipe diameter or channel width for subcooled boiling flow problems can be modeled with reasonable accuracy. This differs greatly from the semi-empirical equi-

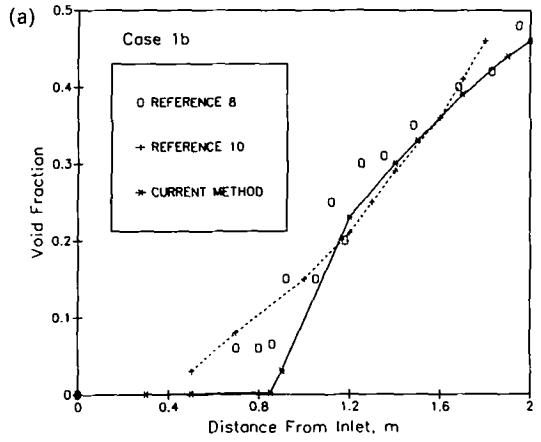

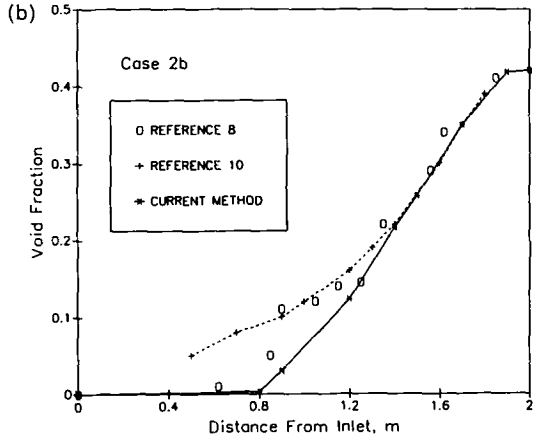

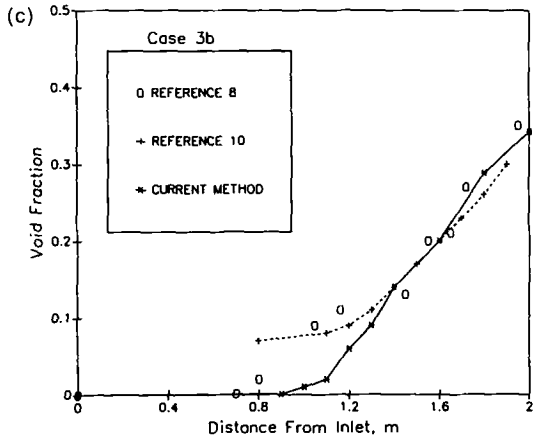

FIG. 14. Comparison of the radially averaged void fraction predictions. (a) Case 1b; (b) case 2b; (c) case 3b.

librium models [3, 10]. One-dimensional analysis is used routinely in the semi-empirical models and thus two-dimensional effects such as the void distribution across the pipe diameter are often not known. The present model attempts to predict the non-equilibrium effect, that is, superheating near the wall and subcooling in the center. Strong radial variations of the vapor and liquid volume fractions are predicted for computations which mimic the experimental conditions of Bartolemei and Chanturiya [8] and St Pierre and Bankoff [9].

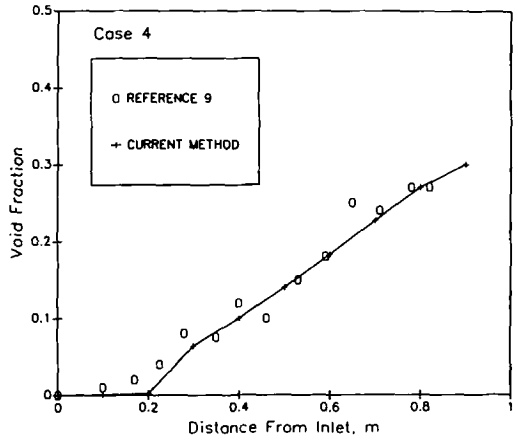

FIG. 15. Comparison of the transversally averaged void fraction predictions for case 4.

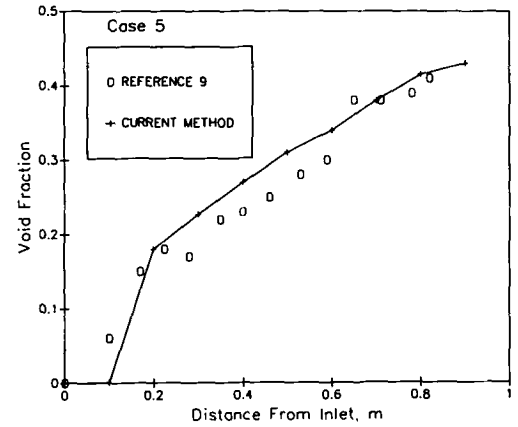

FIG. 16. Comparison of the transversally averaged void fraction predictions for case 5.

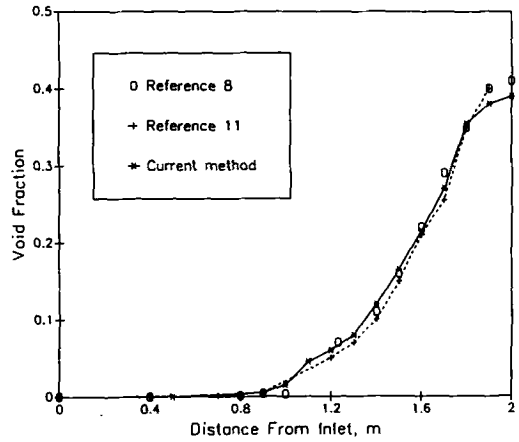

FIG. 17. Comparison of the radially averaged void fraction predictions with the model predictions of Kurul and Podowski [11].

The predicted radial temperature distributions at various axial locations (for the vertical pipe problem)

are in good agreement with experimental data. The predicted transverse void distribution (for the vertical channel problem) at different axial locations show reasonable agreement with the measurements. Improved models are necessary to characterize the physical processes occurring near the wall that affect heat and mass transfer in subcooled boiling.

Radially/transversally averaged properties are obtained from the present two-dimensional predictions and are compared with experimental data. The results from the present method are also compared with those from the one-dimensional semi-empirical model and another two-fluid model. It is concluded that using the simpler but physically based interfacial heat transfer relations near the wall node, the predictions of the two-phase parameters is in agreement with those predicted by using an approach that accounts for boiling from wall surface and the quenching heat flux.

Acknowledgements—The authors would like to thank the Public Service Electric and Gas Company for the partial support of this research study.

REFERENCES

1. S. Levy, Forced-convection subcooled boiling: prediction of vapor volume fraction, *Int. J. Heat Mass Transfer* **10**, 951–965 (1967).
2. F. W. Staub, The void fraction in subcooled boiling: prediction of the initial point of net vapor generation, *J. Heat Transfer, Trans. ASME, Series C* **90**, 151–157 (1968).
3. P. Saha and N. Zuber, Point of net vapor generation and vapor void fraction in subcooled boiling, *Proc. 5th International Heat Transfer Conference, Tokyo*, paper B4.7 (1974).
4. P. Griffith, J. A. Clark and W. M. Rohsenow, Void volumes in subcooled boiling systems, Paper 58-HT-19, presented at ASME–AIChE Heat Transfer Conference, Chicago (1958).
5. R. W. Bowring, Physical model based on bubble detachment and calculation of steam voidage in the subcooled region of a heated channel, OECD Halden Reactor Project Report HPR-10 (1962).
6. J. R. S. Thom, W. W. Walker, T. A. Fallon and G. F. S. Reising, Boiling in subcooled water during flow up heated tubes or annuli, Paper No. 6 presented at the Symposium on Boiling Heat Transfer, IMechE (London), 15–16 September (1965).
7. P. G. Kroeger and N. Zuber, An analysis of the effects of various parameters on the average void fractions in subcooled boiling, *Int. J. Heat Mass Transfer* **11**, 211–233 (1968).
8. C. C. Bartolemei and V. M. Chanturiya, Experimental study of true void fraction when boiling subcooled water in vertical tubes, *Thermal Engng* **14**, 123–128 (1967).
9. C. C. St Pierre and S. G. Bankoff, Vapor volume profiles in developing two-phase flow, *Int. J. Heat Mass Transfer* **10**, 237–249 (1967).
10. P. S. Larsen and L. S. Tong, Void fractions in subcooled flow boiling, *J. Heat Transfer* **November**, 471–476 (1969).
11. M. Z. Podowski and N. Kurul, Multidimensional effects in forced convective subcooled boiling, 9th International Heat Transfer Conference, Jerusalem, August (1990).
12. H. Schlichting, *Boundary Layer Theory* (7th Edn), Chap. 20, p. 610, McGraw-Hill, New York (1979).
13. D. Moalem and B. Sideman, The effects of motion on bubble collapse, *Int. J. Heat Mass Transfer* **16**, 2321–2329 (1973).
14. M. Ishii, Interfacial area modeling, CONF-8509123-1, December (1985).
15. J. Loomis and W. H. Reed, THERMIT-A computer program for three-dimensional thermal-hydraulic analysis of light water reactor cores, NP-2032, EPRI, September (1981).
16. M. J. Thurgood and J. M. Kelly, COBRA/TRAC—a thermal-hydraulics code for transient analysis of nuclear reactor vessels and primary coolant systems, NUREG/CR-3046, Vol. 1, March (1983).
17. M. V. H. Del Valle and D. B. R. Kenning, Subcooled flow boiling at high heat flux, *Int. J. Heat Mass Transfer* **28**, 1907–1920 (1985).
18. H. Rosten and D. B. Spalding, PHOENICS—users' manual, CHAM TR/100 CHAM Limited, 40 High Street, Wimbledon, London, U.K. (1986).
19. D. B. Spalding, Numerical computation of multi-phase fluid flow and heat transfer, EPRI WS-78-143, Vol. 2 (1980).